

# Three-Dimensional Diffraction by Infinite Conducting and Dielectric Wedges Using a Generalized Total-Field/Scattered-Field FDTD Formulation

Jiuan-Her Chang and Allen Taflove, *Fellow, IEEE*

**Abstract**—We extend the generalized total-field/scattered-field formulation of the finite-difference time-domain method to permit efficient computational modeling of three-dimensional (3-D) diffraction by infinite conducting and dielectric wedges. This new method allows: 1) sourcing a numerical plane wave having an arbitrary incident angle traveling into, or originating from, a perfectly matched layer absorbing boundary and 2) terminating the infinite wedge inside the perfectly matched layer with negligible reflection. We validate the new method by comparing its results with the analytical diffraction coefficients for an infinite 3-D right-angle perfect electric conductor wedge obtained using the uniform theory of diffraction. Then, we apply the new method to calculate numerical diffraction coefficients for a 3-D infinite right-angle dielectric wedge, covering a wide range of incident and scattering angles. Finally, we show means to compactly store the calculated diffraction coefficients in a manner which permits easy interpolation of the results for arbitrary incidence and observation angles.

**Index Terms**—Diffraction, finite-difference time-domain (FDTD) method, wedges.

## I. INTRODUCTION

WIRELESS communication systems ideally provide contiguous coverage for mobile users in the geographical areas served. A combination of software planning tools and on-site measurements is used to determine the location and type of radio equipment that is required to achieve this goal. In urban environments, where cells are small, planning tools usually employ deterministic prediction models. Here, accurate estimation of radio wave diffraction from building corners and edges becomes very important. However, existing analytical methods are generally inadequate in calculating electromagnetic wave diffraction from such material wedges. Inaccurate diffraction models could lead to significant errors in RF coverage predictions for cellular systems in urban environments.

In this paper, we extend the generalized total-field/scattered-field (G-TF/SF) formulation [1] of the finite-difference time-domain (FDTD) method [2] to permit efficient computational

modeling of three-dimensional (3-D) diffraction by infinite conducting and dielectric wedges. While a number of recent papers have been published dealing with improvements on the TF/SF formulation (for example [3], [4]), the present work is the first to extend the TF/SF interface into the 3-D perfectly matched layer (PML) absorbing boundary region. This work is an advance relative to the two-dimensional (2-D) technique reported in [1] in that, here, all six vector electromagnetic field components are accounted for at various FDTD space lattice points along and immediately adjacent to the TF/SF interface. Furthermore, we demonstrate how to calibrate the PML in 3-D to numerically obtain the incident field components needed to implement the TF/SF algorithm where the TF/SF interface is embedded within the PML. In essence, we show how to efficiently setup and use an auxiliary 3-D FDTD space lattice to obtain the necessary incident wave data within the PML.

Our new method allows: 1) sourcing a numerical plane wave having an arbitrary incident angle traveling into, or originating from, a perfectly matched layer absorbing boundary and 2) terminating the infinite wedge inside the perfectly matched layer with negligible reflection. We validate the new method by comparing its results with the analytical diffraction coefficients for an infinite 3-D right-angle perfect electric conductor (PEC) wedge obtained using the uniform theory of diffraction (UTD) [5]. Then, we apply the new G-TF/SF method to calculate numerical diffraction coefficients for a 3-D infinite right-angle dielectric wedge, covering a wide range of incident and scattering angles. Finally, we show means to compactly store the calculated diffraction coefficients in a manner which permits easy interpolation of the results for arbitrary incidence and observation angles. This storage/interpolation technique is also a significant advance relative to [1].

## II. GENERAL DESCRIPTION OF THE 3-D G-TF/SF FDTD FORMULATION

The G-TF/SF formulation of the FDTD method permits accurate modeling of an infinite material wedge inside a compact 3-D FDTD grid to efficiently obtain numerical diffraction coefficients. As shown in Fig. 1, the G-TF/SF boundary is located in part within the PML [6] absorbing boundary region of the FDTD grid.

Fig. 2 shows the six faces of the 3-D TF/SF interface of Fig. 1, where a 3-D right-angle wedge is located inside the

Manuscript received June 22, 2004; revised October 6, 2004. This work was performed under a grant from Motorola, Incorporated, Schaumburg, IL, to the Motorola/Northwestern University Center for Communications.

The authors are with the Department of Electrical and Computer Engineering, Northwestern University, Evanston, IL 60208 USA (e-mail: grace@ece.northwestern.edu).

Digital Object Identifier 10.1109/TAP.2005.846359

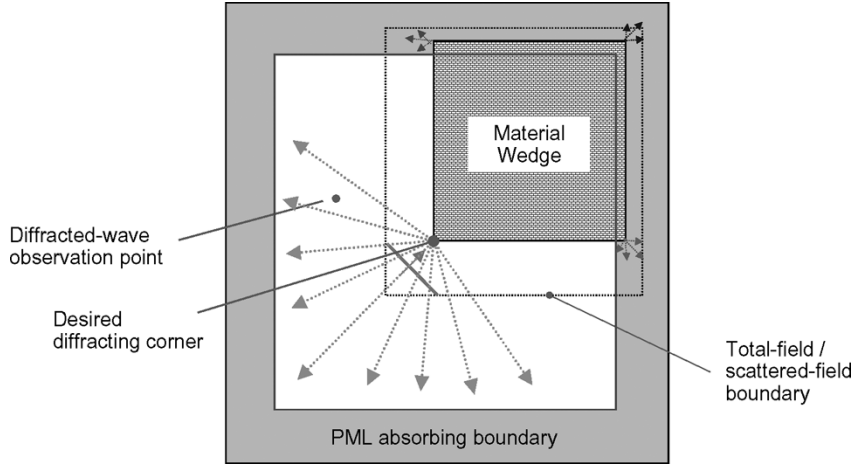


Fig. 1. G-TF/SF formulation of FDTD extends the material wedge into the PML to suppress spurious diffraction. Only diffraction from the desired corner is observed.

G-TF/SF boundary and partially embedded within the PML. An all Berenger split-field PML formulation is assumed for simplicity. The portion of the G-TF/SF surface located inside the PML is indicated by shading. For the special field points along this surface that lie in free space, we use the well-known update equations for the conventional TF/SF boundary [2]. The special field points in the PML absorbing region require special update equations, to be discussed in the following section.

### III. SPECIAL UPDATE EQUATIONS FOR G-TF/SF BOUNDARY IN PML REGION

Referring to Fig. 2(a), we first consider the  $j = j_0$  face of the TF/SF surface inside the PML region, i.e., Regions I and III–VI, for the E-field updates. Here, the special update equation for  $E_{xy}$  is given by:

$j = j_0$  TF/SF Face in PML: [Regions I and III–VI, in Fig. 2(a)]

$$E_{xy,\text{tot}}|_{i,j+\frac{1}{2},k+\frac{1}{2}}^{n+\frac{1}{2}} = C_{a,E_{xy}}^{\text{PML}}|_{i,j+\frac{1}{2},k+\frac{1}{2}} E_{xy,\text{tot}}|_{i,j+\frac{1}{2},k+\frac{1}{2}}^{n-\frac{1}{2}} + C_{b,E_{xy}}^{\text{PML}}|_{i,j+\frac{1}{2},k+\frac{1}{2}} \left[ H_{z,\text{tot}}|_{i,j+1,k+\frac{1}{2}}^n - H_{z,\text{tot}}|_{i,j,k+\frac{1}{2}}^n \right]. \quad (1)$$

Since  $H_{z,\text{tot}}|_{i,j,k+\frac{1}{2}}^n = H_{z,\text{scat}}|_{i,j,k+\frac{1}{2}}^n + H_{z,\text{inc}}|_{i,j,k+\frac{1}{2}}^n$ , therefore

$$E_{xy,\text{tot}}|_{i,j+\frac{1}{2},k+\frac{1}{2}}^{n+\frac{1}{2}} = C_{a,E_{xy}}^{\text{PML}}|_{i,j+\frac{1}{2},k+\frac{1}{2}} E_{xy,\text{tot}}|_{i,j+\frac{1}{2},k+\frac{1}{2}}^{n-\frac{1}{2}} + C_{b,E_{xy}}^{\text{PML}}|_{i,j+\frac{1}{2},k+\frac{1}{2}} \left[ H_{z,\text{tot}}|_{i,j+1,k+\frac{1}{2}}^n - H_{z,\text{scat}}|_{i,j,k+\frac{1}{2}}^n \right] - C_{b,E_{xy}}^{\text{PML}}|_{i,j+\frac{1}{2},k+\frac{1}{2}} H_{z,\text{inc}}|_{i,j,k+\frac{1}{2}}^n \quad (2)$$

Rewriting the above equation in a more convenient form, we have

$$E_{xy,\text{tot}}|_{i,j+\frac{1}{2},k+\frac{1}{2}}^{n+\frac{1}{2}} = \left[ E_{xy,\text{tot}}|_{i,j+\frac{1}{2},k+\frac{1}{2}}^{n+\frac{1}{2}} \right]_{\text{PML}} - C_{b,E_{xy}}^{\text{PML}}|_{i,j+\frac{1}{2},k+\frac{1}{2}} H_{z,\text{inc}}|_{i,j,k+\frac{1}{2}}^n. \quad (3a)$$

Similarly, at this same face of the TF/SF surface in the PML, we have

$$E_{zy,\text{tot}}|_{i-\frac{1}{2},j+\frac{1}{2},k+1}^{n+\frac{1}{2}} = \left[ E_{zy,\text{tot}}|_{i-\frac{1}{2},j+\frac{1}{2},k+1}^{n+\frac{1}{2}} \right]_{\text{PML}} + C_{b,E_{zy}}^{\text{PML}}|_{i-\frac{1}{2},j+\frac{1}{2},k+1} H_{x,\text{inc}}|_{i-\frac{1}{2},j,k+1}^n. \quad (3b)$$

In an analogous manner, we proceed to the other five faces of the TF/SF surface in the PML.

$j = j_1$  TF/SF Face in PML: [Regions I–VI in Fig. 2(b)]

$$E_{xy,\text{tot}}|_{i,j+\frac{1}{2},k+\frac{1}{2}}^{n+\frac{1}{2}} = \left[ E_{xy,\text{tot}}|_{i,j+\frac{1}{2},k+\frac{1}{2}}^{n+\frac{1}{2}} \right]_{\text{PML}} + C_{b,E_{xy}}^{\text{PML}}|_{i,j+\frac{1}{2},k+\frac{1}{2}} \times H_{z,\text{inc}}|_{i,j+1,k+\frac{1}{2}}^n \quad (4a)$$

$$E_{zy,\text{tot}}|_{i-\frac{1}{2},j+\frac{1}{2},k+1}^{n+\frac{1}{2}} = \left[ E_{zy,\text{tot}}|_{i-\frac{1}{2},j+\frac{1}{2},k+1}^{n+\frac{1}{2}} \right]_{\text{PML}} - C_{b,E_{zy}}^{\text{PML}}|_{i-\frac{1}{2},j+\frac{1}{2},k+1} \times H_{x,\text{inc}}|_{i-\frac{1}{2},j+1,k+1}^n \quad (4b)$$

$k = k_0$  TF/SF Face in PML: [Regions I–IV in Fig. 2(c)]

$$E_{xz,\text{tot}}|_{i,j+\frac{1}{2},k+\frac{1}{2}}^{n+\frac{1}{2}} = \left[ E_{xz,\text{tot}}|_{i,j+\frac{1}{2},k+\frac{1}{2}}^{n+\frac{1}{2}} \right]_{\text{PML}} + C_{b,E_{xz}}^{\text{PML}}|_{i,j+\frac{1}{2},k+\frac{1}{2}} \times H_{y,\text{inc}}|_{i,j+\frac{1}{2},k}^n \quad (5a)$$

$$E_{yz,\text{tot}}|_{i-\frac{1}{2},j+1,k+\frac{1}{2}}^{n+\frac{1}{2}} = \left[ E_{yz,\text{tot}}|_{i-\frac{1}{2},j+1,k+\frac{1}{2}}^{n+\frac{1}{2}} \right]_{\text{PML}} - C_{b,E_{yz}}^{\text{PML}}|_{i-\frac{1}{2},j+1,k+\frac{1}{2}} \times H_{x,\text{inc}}|_{i-\frac{1}{2},j+1,k}^n \quad (5b)$$



$i = i_1$  TF/SF Face in PML: [Regions I–VI in Fig. 2(f)]

$$E_{yx,\text{tot}}|_{i-\frac{1}{2},j+1,k+\frac{1}{2}}^{n+\frac{1}{2}} = \left[ E_{yx,\text{tot}}|_{i-\frac{1}{2},j+1,k+\frac{1}{2}}^{n+\frac{1}{2}} \right]_{\text{PML}} - C_{b,E_{yx}}^{\text{PML}}|_{i-\frac{1}{2},j+1,k+\frac{1}{2}} \times H_{z,\text{inc}}|_{i,j+1,k+\frac{1}{2}}^n \quad (8a)$$

$$E_{zx,\text{tot}}|_{i-\frac{1}{2},j+\frac{1}{2},k+1}^{n+\frac{1}{2}} = \left[ E_{zx,\text{tot}}|_{i-\frac{1}{2},j+\frac{1}{2},k+1}^{n+\frac{1}{2}} \right]_{\text{PML}} + C_{b,E_{zx}}^{\text{PML}}|_{i-\frac{1}{2},j+\frac{1}{2},k+1} \times H_{y,\text{inc}}|_{i,j+\frac{1}{2},k+1}^n \quad (8b)$$

Equations (3)–(8) represent the complete set of special electric-field update equations required to implement the 3-D generalized TF/SF boundary of Figs. 1 and 2.

Next, we consider the  $j = j_0 - 1/2$  face adjacent to the TF/SF surface inside the PML for the required H-field updates. Here, the special update equation for  $H_{zy}$  is given by:

$j = j_0 - 1/2$  Face in PML: [Adjacent to regions I and III–VI in Fig. 2(a)]

$$H_{zy,\text{scat}}|_{i,j+1,k+\frac{1}{2}}^{n+1} = D_{a,H_{zy}}^{\text{PML}}|_{i,j+1,k+\frac{1}{2}} H_{zy,\text{scat}}|_{i,j+1,k+\frac{1}{2}}^n + D_{b,H_{zy}}^{\text{PML}}|_{i,j+1,k+\frac{1}{2}} \times \left[ E_{x,\text{scat}}|_{i,j+\frac{3}{2},k+\frac{1}{2}}^{n+\frac{1}{2}} - E_{x,\text{scat}}|_{i,j+\frac{1}{2},k+\frac{1}{2}}^{n+\frac{1}{2}} \right]. \quad (9)$$

Since  $E_{x,\text{scat}}|_{i,j+3/2,k+1/2}^{n+1/2} = E_{x,\text{tot}}|_{i,j+3/2,k+1/2}^{n+1/2} - E_{x,\text{inc}}|_{i,j+3/2,k+1/2}^{n+1/2}$ , therefore

$$H_{zy,\text{scat}}|_{i,j+1,k+\frac{1}{2}}^{n+1} = \left[ H_{zy,\text{scat}}|_{i,j+1,k+\frac{1}{2}}^{n+1} \right]_{\text{PML}} - D_{b,H_{zy}}^{\text{PML}}|_{i,j+1,k+\frac{1}{2}} E_{x,\text{inc}}|_{i,j+\frac{3}{2},k+\frac{1}{2}}^{n+\frac{1}{2}}. \quad (10a)$$

Similarly, at this same face adjacent to the TF/SF surface in the PML, we have

$$H_{xy,\text{scat}}|_{i-\frac{1}{2},j+1,k+1}^{n+1} = \left[ H_{xy,\text{scat}}|_{i-\frac{1}{2},j+1,k+1}^{n+1} \right]_{\text{PML}} + D_{b,H_{xy}}^{\text{PML}}|_{i-\frac{1}{2},j+1,k+1} E_{z,\text{inc}}|_{i-\frac{1}{2},j+\frac{3}{2},k+1}^{n+\frac{1}{2}}. \quad (10b)$$

In an analogous manner, we proceed to the other five faces adjacent to the TF/SF surface in the PML:

$j = j_1 + 1/2$  Face in PML: [Adjacent to regions I–VI in Fig. 2(b)]

$$H_{zy,\text{scat}}|_{i,j+1,k+\frac{1}{2}}^{n+1} = \left[ H_{zy,\text{scat}}|_{i,j+1,k+\frac{1}{2}}^{n+1} \right]_{\text{PML}} + D_{b,H_{zy}}^{\text{PML}}|_{i,j+1,k+\frac{1}{2}} \times E_{x,\text{inc}}|_{i,j+\frac{1}{2},k+\frac{1}{2}}^{n+\frac{1}{2}} \quad (11a)$$

$$H_{xy,\text{scat}}|_{i-\frac{1}{2},j+1,k+1}^{n+1} = \left[ H_{xy,\text{scat}}|_{i-\frac{1}{2},j+1,k+1}^{n+1} \right]_{\text{PML}} - D_{b,H_{xy}}^{\text{PML}}|_{i-\frac{1}{2},j+1,k+1} \times E_{z,\text{inc}}|_{i-\frac{1}{2},j+\frac{1}{2},k+1}^{n+\frac{1}{2}} \quad (11b)$$

$k = k_0 - 1/2$  Face in PML: [Adjacent to regions I–IV in Fig. 2(c)]

$$H_{yz,\text{scat}}|_{i,j+\frac{1}{2},k+1}^{n+1} = \left[ H_{yz,\text{scat}}|_{i,j+\frac{1}{2},k+1}^{n+1} \right]_{\text{PML}} + D_{b,H_{yz}}^{\text{PML}}|_{i,j+\frac{1}{2},k+1} \times E_{x,\text{inc}}|_{i,j+\frac{1}{2},k+\frac{3}{2}}^{n+\frac{1}{2}} \quad (12a)$$

$$H_{xz,\text{scat}}|_{i-\frac{1}{2},j+1,k+1}^{n+1} = \left[ H_{xz,\text{scat}}|_{i-\frac{1}{2},j+1,k+1}^{n+1} \right]_{\text{PML}} - D_{b,H_{xz}}^{\text{PML}}|_{i-\frac{1}{2},j+1,k+1} \times E_{y,\text{inc}}|_{i-\frac{1}{2},j+1,k+\frac{3}{2}}^{n+\frac{1}{2}} \quad (12b)$$

$k = k_1 + 1/2$  Face in PML: [Adjacent to regions I–IV in Fig. 2(d)]

$$H_{yz,\text{scat}}|_{i,j+\frac{1}{2},k+1}^{n+1} = \left[ H_{yz,\text{scat}}|_{i,j+\frac{1}{2},k+1}^{n+1} \right]_{\text{PML}} - D_{b,H_{yz}}^{\text{PML}}|_{i,j+\frac{1}{2},k+1} \times E_{x,\text{inc}}|_{i,j+\frac{1}{2},k+\frac{1}{2}}^{n+\frac{1}{2}} \quad (13a)$$

$$H_{xz,\text{scat}}|_{i-\frac{1}{2},j+1,k+1}^{n+1} = \left[ H_{xz,\text{scat}}|_{i-\frac{1}{2},j+1,k+1}^{n+1} \right]_{\text{PML}} + D_{b,H_{xz}}^{\text{PML}}|_{i-\frac{1}{2},j+1,k+1} \times E_{y,\text{inc}}|_{i-\frac{1}{2},j+1,k+\frac{1}{2}}^{n+\frac{1}{2}} \quad (13b)$$

$i = i_0 - 1/2$  Face in PML: [Adjacent to regions I and III–VI in Fig. 2(e)]

$$H_{zx,\text{scat}}|_{i,j+1,k+\frac{1}{2}}^{n+1} = \left[ H_{zx,\text{scat}}|_{i,j+1,k+\frac{1}{2}}^{n+1} \right]_{\text{PML}} + D_{b,H_{zx}}^{\text{PML}}|_{i,j+1,k+\frac{1}{2}} \times E_{y,\text{inc}}|_{i+\frac{1}{2},j+1,k+\frac{1}{2}}^{n+\frac{1}{2}} \quad (14a)$$

$$H_{yx,\text{scat}}|_{i,j+\frac{1}{2},k+1}^{n+1} = \left[ H_{yx,\text{scat}}|_{i,j+\frac{1}{2},k+1}^{n+1} \right]_{\text{PML}} - D_{b,H_{yx}}^{\text{PML}}|_{i,j+\frac{1}{2},k+1} \times E_{z,\text{inc}}|_{i+\frac{1}{2},j+\frac{1}{2},k+1}^{n+\frac{1}{2}} \quad (14b)$$

$i = i_1 + 1/2$  Face in PML: [Adjacent to regions I–VI in Fig. 2(f)]

$$H_{zx,\text{scat}}|_{i,j+1,k+\frac{1}{2}}^{n+1} = \left[ H_{zx,\text{scat}}|_{i,j+1,k+\frac{1}{2}}^{n+1} \right]_{\text{PML}} - D_{b,H_{zx}}^{\text{PML}}|_{i,j+1,k+\frac{1}{2}} \times E_{y,\text{inc}}|_{i-\frac{1}{2},j+1,k+\frac{1}{2}}^{n+\frac{1}{2}} \quad (15a)$$

$$H_{yx,\text{scat}}|_{i,j+\frac{1}{2},k+1}^{n+1} = \left[ H_{yx,\text{scat}}|_{i,j+\frac{1}{2},k+1}^{n+1} \right]_{\text{PML}} + D_{b,H_{yx}}^{\text{PML}}|_{i,j+\frac{1}{2},k+1} \times E_{z,\text{inc}}|_{i-\frac{1}{2},j+\frac{1}{2},k+1}^{n+\frac{1}{2}}. \quad (15b)$$

Equations (10)–(15) represent a complete set of special magnetic-field update equations required to implement the generalized TF/SF boundary of Figs. 1 and 2. These equations, as well

as (3) to (8) can be implemented as long as we know the appropriate incident fields in the PML. Note that all of these equations, knowledge of the *total* incident field components ( $E_{xy} + E_{xz}$ ), etc., and not the individual split incident field is required.

#### IV. CALIBRATION PROCESS

In this section, we discuss the method to obtain the incident E and H field components in the PML region that are required in (3)–(8) and (10)–(15).

We cannot assume a perfect exponential decay of the incident wave in the PML region. For accuracy, this decay must be obtained numerically in a calibration process

$$\psi_{\text{inc}}^{\text{num}} = X_0^{\text{num}} A_{\text{PML}}(\theta_{\text{inc}}, \phi_{\text{inc}}). \quad (16)$$

Here,  $\psi_{\text{inc}}^{\text{num}}$  represents the required incident E or H field component at an observation point in the PML region,  $X_0^{\text{num}}$  is the corresponding free space incident field (which can be obtained using the table look-up procedure of [2]);  $A_{\text{PML}}$  is an appropriate multiplying factor to be determined in the calibration process and  $(\theta_{\text{inc}}, \phi_{\text{inc}})$  is the direction of the incident plane wave.

For a given FDTD grid configuration and an arbitrary  $(\theta_{\text{inc}}, \phi_{\text{inc}})$ ,  $A_{\text{PML}}$  is obtained by conducting preliminary FDTD runs to calibrate the performance of the PML. In these runs, we illuminate the desired PML region of the grid with a pulsed incident plane wave having a desired center frequency,  $f_o$ , and full-width at half-maximum (FWHM) bandwidth,  $\Delta f$ . We record the amplitude of the E and H field components within the PML,  $F_{o,\text{inc}}^{\text{PML}}(\theta_{\text{inc}}, \phi_{\text{inc}}, d)$  at each required depth,  $d$ . We also compute the amplitude of the corresponding incident electric and magnetic fields,  $F_{o,\text{inc}}^{\text{freespace}}(\theta_{\text{inc}}, \phi_{\text{inc}}, d)$ , in free space. Then, for a wave impinging upon a given PML region, we define the attenuation factor,  $Attn_{\text{PML}}(\theta_{\text{inc}}, \phi_{\text{inc}}, d)$ , as

$$Attn_{\text{PML}}(\theta_{\text{inc}}, \phi_{\text{inc}}, d) = \frac{F_{o,\text{inc}}^{\text{PML}}(\theta_{\text{inc}}, \phi_{\text{inc}}, d)}{F_{o,\text{inc}}^{\text{freespace}}(\theta_{\text{inc}}, \phi_{\text{inc}}, d)}. \quad (17a)$$

Similarly, for a wave originating within a given PML region, we define the amplification factor,  $Ampf_{\text{PML}}(\theta_{\text{inc}}, \phi_{\text{inc}}, d)$ , as

$$Ampf_{\text{PML}}(\theta_{\text{inc}}, \phi_{\text{inc}}, d) = \frac{F_{o,\text{inc}}^{\text{freespace}}(\pi + \theta_{\text{inc}}, \pi + \phi_{\text{inc}}, d)}{F_{o,\text{inc}}^{\text{PML}}(\pi + \theta_{\text{inc}}, \pi + \phi_{\text{inc}}, d)}. \quad (17b)$$

Note that  $Ampf_{\text{PML}}(\theta_{\text{inc}}, \phi_{\text{inc}}, d)$  is obtained in the preliminary FDTD run by illuminating the given PML region with a plane wave incident at  $(\theta_{\text{inc}} + 180^\circ, \phi_{\text{inc}} + 180^\circ)$ .

We now summarize the calibration procedure. For each required incident direction  $(\theta_{\text{inc}}, \phi_{\text{inc}})$ , we set up three preliminary FDTD calibration runs to obtain  $A_{\text{PML}}(\theta_{\text{inc}}, \phi_{\text{inc}})$  in  $+x$ ,  $+y$ ,  $+z$  PML regions. In the preliminary FDTD runs we launch an approximate plane wave impinging upon the local PML region of interest by exciting a nearby parallel TF/SF boundary plane. For example, to obtain the calibration for a plane wave penetrating into the  $+y$  PML region, we use a nearby TF/SF boundary having only an  $x - z$  face, and observe penetration into the PML at points away from the edges of the face. Here, in one preliminary run, we obtain  $Attn_{y,\text{PML}}$  and  $Ampf_{y,\text{PML}}$

for all PML depths ( $d_y$ ) in the  $+y$  PML region. Correspondingly, in another two preliminary runs we obtain  $Attn_{x,\text{PML}}$ ,  $Ampf_{x,\text{PML}}$ ,  $Attn_{z,\text{PML}}$ , and  $Ampf_{z,\text{PML}}$  for all PML depths ( $d_x, d_z$ ) in the  $+x$  and  $+z$  PML region.

We can now obtain  $A_{\text{PML}}$  from  $Attn_{x,\text{PML}}$ ,  $Ampf_{x,\text{PML}}$ ,  $Attn_{y,\text{PML}}$ ,  $Ampf_{y,\text{PML}}$ ,  $Attn_{z,\text{PML}}$ , and  $Ampf_{z,\text{PML}}$  for all G-TF/SF boundary segments in PML, and all angles of incidence. For example, referring to Fig. 2; consider the  $j = j_1$  face:

For  $0^\circ < \theta_{\text{inc}} \leq 90^\circ$ ,

Region I:

$$A_{\text{PML}} = A_{y,\text{PML}}(j_1) A_{z,\text{PML}}(z) = \begin{cases} Attn_{y,\text{PML}}(j_1) \\ \times Attn_{z,\text{PML}}(z) & 0^\circ < \phi_{\text{inc}} \leq 180^\circ \\ Ampf_{y,\text{PML}}(j_1) \\ \times Attn_{z,\text{PML}}(z) & 180^\circ < \phi_{\text{inc}} \leq 360^\circ \end{cases} \quad (18a)$$

where  $k_1^{\text{PML}} \leq z \leq k_1$

Region II:

$$A_{\text{PML}} = A_{y,\text{PML}}(j_1) = \begin{cases} Attn_{y,\text{PML}}(j_1) & 0^\circ < \phi_{\text{inc}} \leq 180^\circ \\ Ampf_{y,\text{PML}}(j_1) & 180^\circ < \phi_{\text{inc}} \leq 360^\circ \end{cases} \quad (18b)$$

Region III:

$$A_{\text{PML}} = A_{y,\text{PML}}(j_1) A_{z,\text{PML}}(z) = \begin{cases} Attn_{y,\text{PML}}(j_1) \\ \times Ampf_{z,\text{PML}}(z) & 0^\circ < \phi_{\text{inc}} \leq 180^\circ \\ Ampf_{y,\text{PML}}(j_1) \\ \times Ampf_{z,\text{PML}}(z) & 180^\circ < \phi_{\text{inc}} \leq 360^\circ \end{cases} \quad (18c)$$

where  $k_0 \leq z \leq k_0^{\text{PML}}$

Region IV:

$$A_{\text{PML}} = A_{x,\text{PML}}(x) A_{y,\text{PML}}(j_1) A_{z,\text{PML}}(z) = \begin{cases} Attn_{x,\text{PML}}(x) Attn_{y,\text{PML}}(j_1) \\ \times Attn_{z,\text{PML}}(z) & 0^\circ < \phi_{\text{inc}} \leq 90^\circ \\ Ampf_{x,\text{PML}}(x) Attn_{y,\text{PML}}(j_1) \\ \times Attn_{z,\text{PML}}(z) & 90^\circ < \phi_{\text{inc}} \leq 180^\circ \\ Ampf_{x,\text{PML}}(x) Ampf_{y,\text{PML}}(j_1) \\ \times Attn_{z,\text{PML}}(z) & 180^\circ < \phi_{\text{inc}} \leq 270^\circ \\ Attn_{x,\text{PML}}(x) Ampf_{y,\text{PML}}(j_1) \\ \times Attn_{z,\text{PML}}(z) & 270^\circ < \phi_{\text{inc}} \leq 360^\circ \end{cases} \quad (18d)$$

where  $i_1^{\text{PML}} \leq x \leq i_1$  and where  $k_1^{\text{PML}} \leq z \leq k_1$

Region V:

$$A_{\text{PML}} = A_{x,\text{PML}}(x) A_{y,\text{PML}}(j_1) = \begin{cases} Attn_{x,\text{PML}}(x) \\ \times Attn_{y,\text{PML}}(j_1) & 0^\circ < \phi_{\text{inc}} \leq 90^\circ \\ Ampf_{x,\text{PML}}(x) \\ \times Attn_{y,\text{PML}}(j_1) & 90^\circ < \phi_{\text{inc}} \leq 180^\circ \\ Ampf_{x,\text{PML}}(x) \\ \times Ampf_{y,\text{PML}}(j_1) & 180^\circ < \phi_{\text{inc}} \leq 270^\circ \\ Attn_{x,\text{PML}}(x) \\ \times Ampf_{y,\text{PML}}(j_1) & 270^\circ < \phi_{\text{inc}} \leq 360^\circ \end{cases} \quad (18e)$$

where  $i_1^{\text{PML}} \leq x \leq i_1$

Region VI:

$$\begin{aligned}
 A_{\text{PML}} &= A_{x,\text{PML}}(x)A_{y,\text{PML}}(j_1)A_{z,\text{PML}}(z) \\
 &= \begin{cases} \text{Attn}_{x,\text{PML}}(x)\text{Attn}_{y,\text{PML}}(j_1) \\ \quad \times \text{Ampf}_{z,\text{PML}}(z) & 0^\circ < \phi_{\text{inc}} \leq 90^\circ \\ \text{Ampf}_{x,\text{PML}}(x)\text{Attn}_{y,\text{PML}}(j_1) \\ \quad \times \text{Ampf}_{z,\text{PML}}(z) & 90^\circ < \phi_{\text{inc}} \leq 180^\circ \\ \text{Ampf}_{x,\text{PML}}(x)\text{Ampf}_{y,\text{PML}}(j_1) \\ \quad \times \text{Ampf}_{z,\text{PML}}(z) & 180^\circ < \phi_{\text{inc}} \leq 270^\circ \\ \text{Attn}_{x,\text{PML}}(x)\text{Ampf}_{y,\text{PML}}(j_1) \\ \quad \times \text{Ampf}_{z,\text{PML}}(z) & 270^\circ < \phi_{\text{inc}} \leq 360^\circ \end{cases} \quad (18f)
 \end{aligned}$$

where  $i_1^{\text{PML}} \leq x \leq i_1$  and  $k_0 \leq z \leq k_0^{\text{PML}}$

For  $90^\circ < \theta_{\text{inc}} < 180^\circ$ ,

Region I:

$$\begin{aligned}
 A_{\text{PML}} &= A_{y,\text{PML}}(j_1)A_{z,\text{PML}}(z) \\
 &= \begin{cases} \text{Attn}_{y,\text{PML}}(j_1) \\ \quad \times \text{Ampf}_{z,\text{PML}}(z) & 0^\circ < \phi_{\text{inc}} \leq 180^\circ \\ \text{Ampf}_{y,\text{PML}}(j_1) \\ \quad \times \text{Ampf}_{z,\text{PML}}(z) & 180^\circ < \phi_{\text{inc}} \leq 360^\circ \end{cases} \quad (19a)
 \end{aligned}$$

where  $k_1^{\text{PML}} \leq z \leq k_1$

Region II:

$$\begin{aligned}
 A_{\text{PML}} &= A_{y,\text{PML}}(j_1) \\
 &= \begin{cases} \text{Attn}_{y,\text{PML}}(j_1) & 0^\circ < \phi_{\text{inc}} \leq 180^\circ \\ \text{Ampf}_{y,\text{PML}}(j_1) & 180^\circ < \phi_{\text{inc}} \leq 360^\circ \end{cases} \quad (19b)
 \end{aligned}$$

Region III:

$$\begin{aligned}
 A_{\text{PML}} &= A_{y,\text{PML}}(j_1)A_{z,\text{PML}}(z) \\
 &= \begin{cases} \text{Attn}_{y,\text{PML}}(j_1) \\ \quad \times \text{Attn}_{z,\text{PML}}(z) & 0^\circ < \phi_{\text{inc}} \leq 180^\circ \\ \text{Ampf}_{y,\text{PML}}(j_1) \\ \quad \times \text{Attn}_{z,\text{PML}}(z) & 180^\circ < \phi_{\text{inc}} \leq 360^\circ \end{cases} \quad (19c)
 \end{aligned}$$

where  $k_0 \leq z \leq k_0^{\text{PML}}$

Region IV:

$$\begin{aligned}
 A_{\text{PML}} &= A_{x,\text{PML}}(x)A_{y,\text{PML}}(j_1)A_{z,\text{PML}}(z) \\
 &= \begin{cases} \text{Attn}_{x,\text{PML}}(x)\text{Attn}_{y,\text{PML}}(j_1) \\ \quad \times \text{Ampf}_{z,\text{PML}}(z) & 0^\circ < \phi_{\text{inc}} \leq 90^\circ \\ \text{Ampf}_{x,\text{PML}}(x)\text{Attn}_{y,\text{PML}}(j_1) \\ \quad \times \text{Ampf}_{z,\text{PML}}(z) & 90^\circ < \phi_{\text{inc}} \leq 180^\circ \\ \text{Ampf}_{x,\text{PML}}(x)\text{Ampf}_{y,\text{PML}}(j_1) \\ \quad \times \text{Ampf}_{z,\text{PML}}(z) & 180^\circ < \phi_{\text{inc}} \leq 270^\circ \\ \text{Attn}_{x,\text{PML}}(x)\text{Ampf}_{y,\text{PML}}(j_1) \\ \quad \times \text{Ampf}_{z,\text{PML}}(z) & 270^\circ < \phi_{\text{inc}} \leq 360^\circ \end{cases} \quad (19d)
 \end{aligned}$$

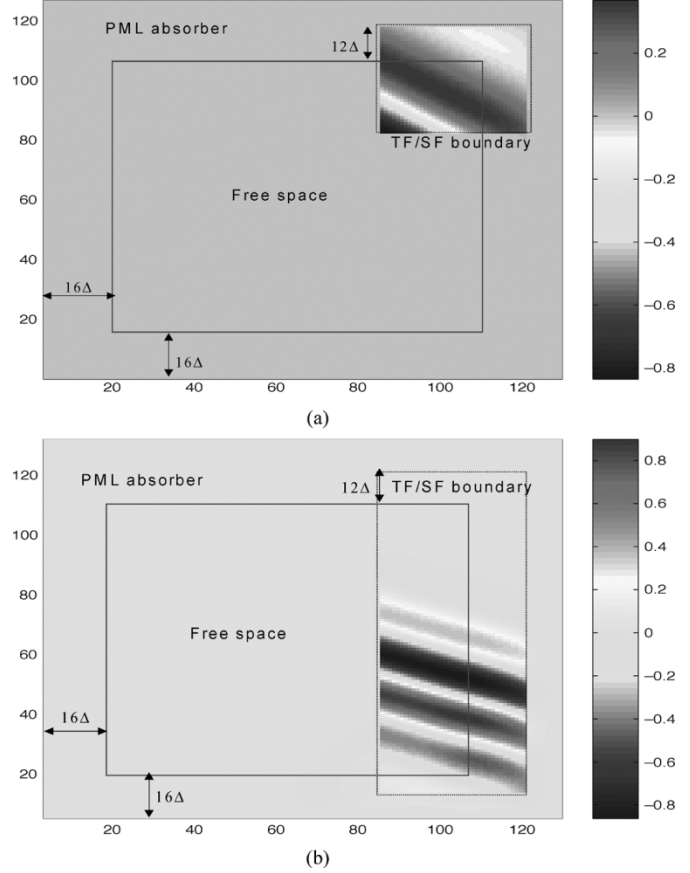


Fig. 3. Snapshot visualizations of a Gaussian pulsed sinusoidal plane wave launched within an empty 3-D total-field zone that extends into PML. (a) Horizontal cut through the space lattice. (b) Vertical cut through the space lattice.

where  $i_1^{\text{PML}} \leq x \leq i_1$  and  $k_1^{\text{PML}} \leq z \leq k_1$

Region V:

$$\begin{aligned}
 A_{\text{PML}} &= A_{x,\text{PML}}(x)A_{y,\text{PML}}(j_1) \\
 &= \begin{cases} \text{Attn}_{x,\text{PML}}(x) \\ \quad \times \text{Attn}_{y,\text{PML}}(j_1) & 0^\circ < \phi_{\text{inc}} \leq 90^\circ \\ \text{Ampf}_{x,\text{PML}}(x) \\ \quad \times \text{Attn}_{y,\text{PML}}(j_1) & 90^\circ < \phi_{\text{inc}} \leq 180^\circ \\ \text{Ampf}_{x,\text{PML}}(x) \\ \quad \times \text{Ampf}_{y,\text{PML}}(j_1) & 180^\circ < \phi_{\text{inc}} \leq 270^\circ \\ \text{Attn}_{x,\text{PML}}(x) \\ \quad \times \text{Ampf}_{y,\text{PML}}(j_1) & 270^\circ < \phi_{\text{inc}} \leq 360^\circ \end{cases} \quad (19e)
 \end{aligned}$$

where  $i_1^{\text{PML}} \leq x \leq i_1$

Region VI:

$$\begin{aligned}
 A_{\text{PML}} &= A_{x,\text{PML}}(x)A_{y,\text{PML}}(j_1)A_{z,\text{PML}}(z) \\
 &= \begin{cases} \text{Attn}_{x,\text{PML}}(x)\text{Attn}_{y,\text{PML}}(j_1) \\ \quad \times \text{Attn}_{z,\text{PML}}(z) & 0^\circ < \phi_{\text{inc}} \leq 90^\circ \\ \text{Ampf}_{x,\text{PML}}(x)\text{Attn}_{y,\text{PML}}(j_1) \\ \quad \times \text{Attn}_{z,\text{PML}}(z) & 90^\circ < \phi_{\text{inc}} \leq 180^\circ \\ \text{Ampf}_{x,\text{PML}}(x)\text{Ampf}_{y,\text{PML}}(j_1) \\ \quad \times \text{Attn}_{z,\text{PML}}(z) & 180^\circ < \phi_{\text{inc}} \leq 270^\circ \\ \text{Attn}_{x,\text{PML}}(x)\text{Ampf}_{y,\text{PML}}(j_1) \\ \quad \times \text{Attn}_{z,\text{PML}}(z) & 270^\circ < \phi_{\text{inc}} \leq 360^\circ \end{cases} \quad (19f)
 \end{aligned}$$

where  $i_1^{\text{PML}} \leq x \leq i_1$  and  $k_0 \leq z \leq k_0^{\text{PML}}$ .

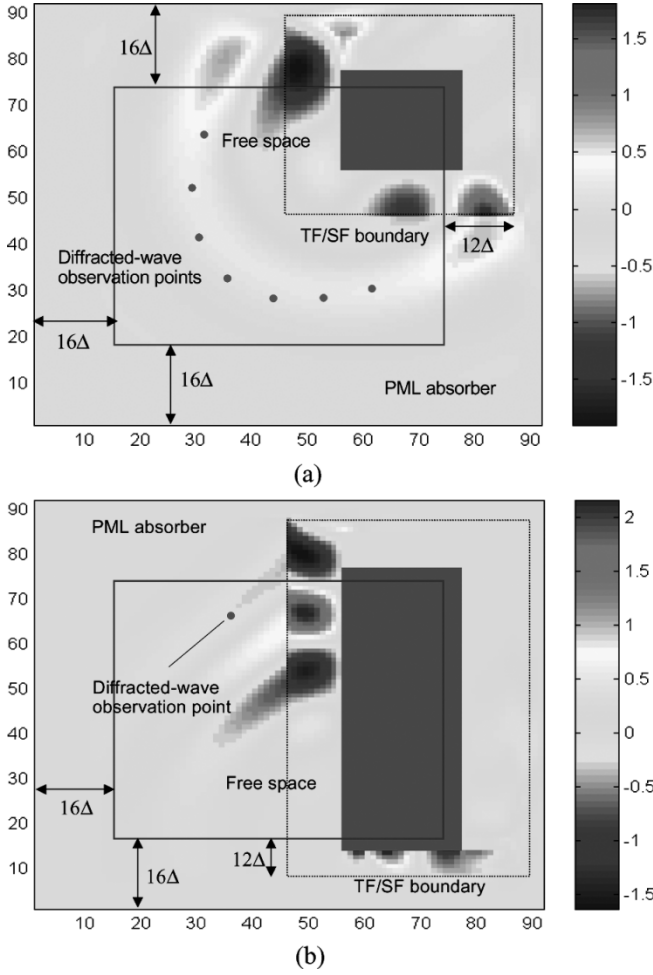


Fig. 4. Snapshot visualizations of a Gaussian pulsed sinusoidal plane wave illuminating a right-angle PEC wedge that extends into PML. (a) Horizontal cut through the space lattice. (b) Vertical cut through the space lattice.

The  $A_{\text{PML}}$  of  $j = j_o, k = k_o, k = k_1, i = i_o, i = i_1$  faces can be obtained by analogy [7]. We use the above equations and (16) to obtain the incident E and H field components at any point in the PML region. We then use the special update (3)–(8) and (10)–(15) to implement the G-TF/SF boundary in the PML.

## V. NUMERICAL RESULTS FOR THREE DIMENSIONAL SCATTERING

### A. Empty Total-Field Zone

We first demonstrate how the G-TF/SF formulation allows launching a numerical plane wave within an empty 3-D total-field zone that extends into PML. Fig. 3 is a snapshot visualization of a Gaussian pulsed sinusoidal plane wave propagating at  $\theta_{\text{inc}} = 35^\circ, \phi_{\text{inc}} = 55^\circ$ . The center frequency is  $f_o = 850$  MHz and the full width at half maximum (FWHM) bandwidth  $\Delta f = 600$  MHz. Here, three preliminary calibration runs were required to obtain  $\text{Attn}_{x,\text{PML}}, \text{Amp}f_{x,\text{PML}}, \text{Attn}_{y,\text{PML}}, \text{Amp}f_{y,\text{PML}}, \text{Attn}_{z,\text{PML}},$  and  $\text{Amp}f_{z,\text{PML}}$  for all PML depths ( $d_x, d_y, d_z$ ). From Fig. 3, we see that the propagating wave generated by the G-TF/SF technique maintains its plane nature despite the presence of the PML. Further, the wave is well confined within the TF zone, with little external leakage.

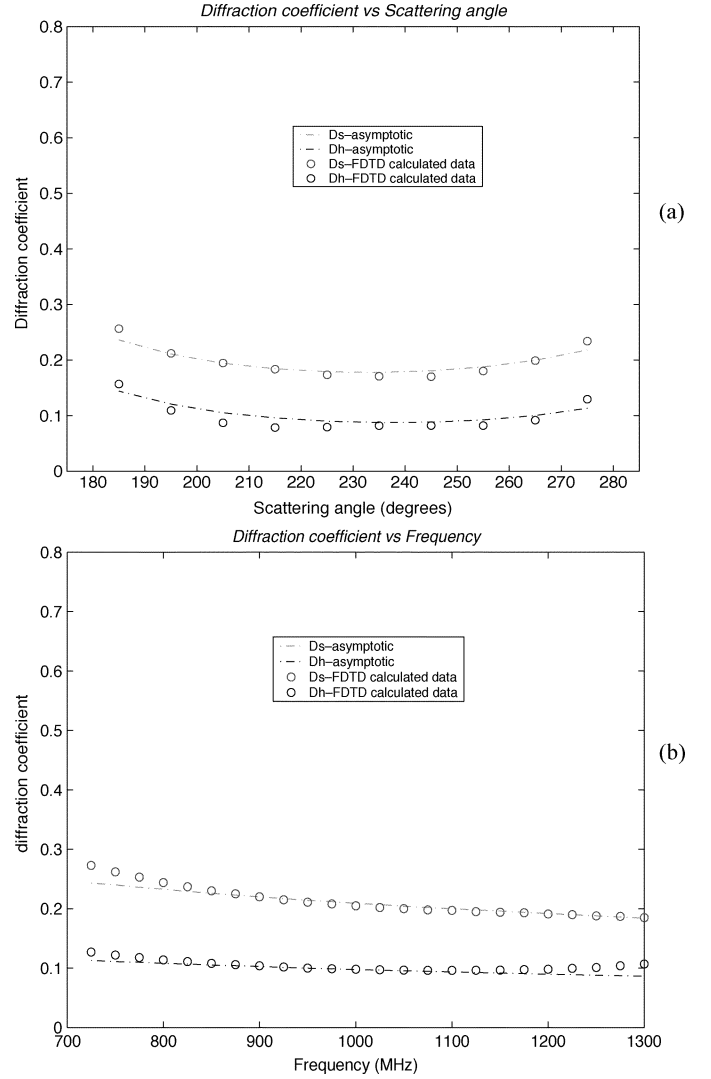


Fig. 5. Comparison of G-TF/SF FDTD and UTD results for the diffraction coefficient of a right-angle PEC wedge. (a) At 850 MHz as a function of scattering angle  $\phi_{\text{scat}}$  for fixed  $\theta_{\text{scat}} = 30^\circ, \theta_{\text{inc}} = 55^\circ,$  and  $\phi_{\text{inc}} = 35^\circ$ . (b) As a function of frequency for  $\theta_{\text{scat}} = 30^\circ, \phi_{\text{scat}} = 165^\circ, \theta_{\text{inc}} = 55^\circ,$  and  $\phi_{\text{inc}} = 65^\circ$ .

### B. Right-Angle PEC Wedge in Total-Field Zone

We next apply the G-TF/SF technique to calculate the diffraction coefficients for an infinite right-angle PEC wedge. The 3-D geometry of the wedge in the FDTD grid and sample field visualizations are shown in Fig. 4. Here, the incident illumination is a Gaussian pulsed plane wave with  $f_o = 850$  MHz and  $\Delta f = 600$  MHz. The diffracted wave observation points are marked in the scattered-field region outside of the TF/SF boundary. FDTD grid resolution equals  $\lambda_o/25$ , where  $\lambda_o$  is the wavelength at 850 MHz.

Fig. 5(a) and (b) compares the G-TF/SF FDTD-computed diffraction coefficients for the infinite PEC wedge of Fig. 4 with the UTD asymptotic results for the corresponding infinite wedge (see [8] and Appendices A and B). Fig. 5(a) shows the variation of the amplitude of the soft and hard diffraction coefficients at  $f_o = 850$  MHz as a function of the observation angle  $\phi_{\text{scat}}$  at a fixed  $\theta_{\text{scat}} = 30^\circ$  and a fixed observation distance  $s \approx 3\lambda_o$  from the diffracting corner. Here, the incident wave propagates

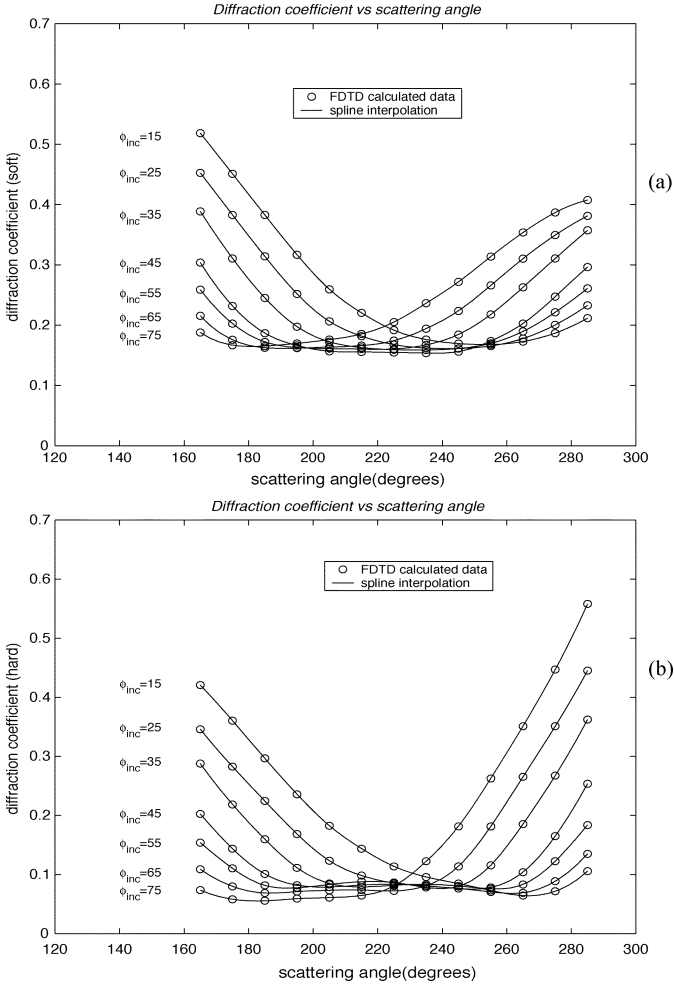


Fig. 6. G-TF/SF FDTD diffraction coefficients for a right-angle lossless dielectric wedge ( $\epsilon_r = 6$ ). 850-MHz incident plane wave at  $\theta_{inc} = 55^\circ$ . (a) Soft diffraction coefficients. (b) Hard diffraction coefficients.

at ( $\theta_{inc} = 55^\circ$ ,  $\phi_{inc} = 35^\circ$ ). Fig. 5(b) shows the variation of the amplitude of the soft and hard diffraction coefficients as a function of frequency at a fixed observation point ( $\theta_{scat} = 30^\circ$ ,  $\phi_{scat} = 165^\circ$ ,  $s \approx 3\lambda_o$ ) over the frequency range 700 MHz to 1.3 GHz for the incident plane wave propagating at ( $\theta_{inc} = 55^\circ$ ,  $\phi_{inc} = 65^\circ$ ). Both figures show very good agreement of the G-TF/SF FDTD results and the asymptotic UTD calculations.

### C. Right-Angle Dielectric Wedge in Total-Field Zone

We now demonstrate the capability of the G-TF/SF FDTD technique to calculate 3-D diffraction coefficients for an infinite lossless right-angle dielectric wedge. The FDTD grid geometry remains that of Fig. 4, but the finite PEC wedge is replaced by a finite lossless dielectric wedge of permittivity  $\epsilon_r = 6$ .

Fig. 6(a) and (b) shows multiple curves for the G-TF/SF FDTD-calculated soft and hard diffraction coefficients at  $f_o = 850$  MHz for plane waves at incident angles  $15^\circ \leq \phi_{inc} \leq 75^\circ$  and observation angles  $160^\circ < \phi_{scat} < 290^\circ$ . In both cases  $\theta_{inc} = 55^\circ$ . We ensure that the distance  $\rho$  from the vertex of the wedge to each observation point is greater than  $2\lambda_o$ , where  $\lambda_o$  is the wavelength at  $f_o$ .

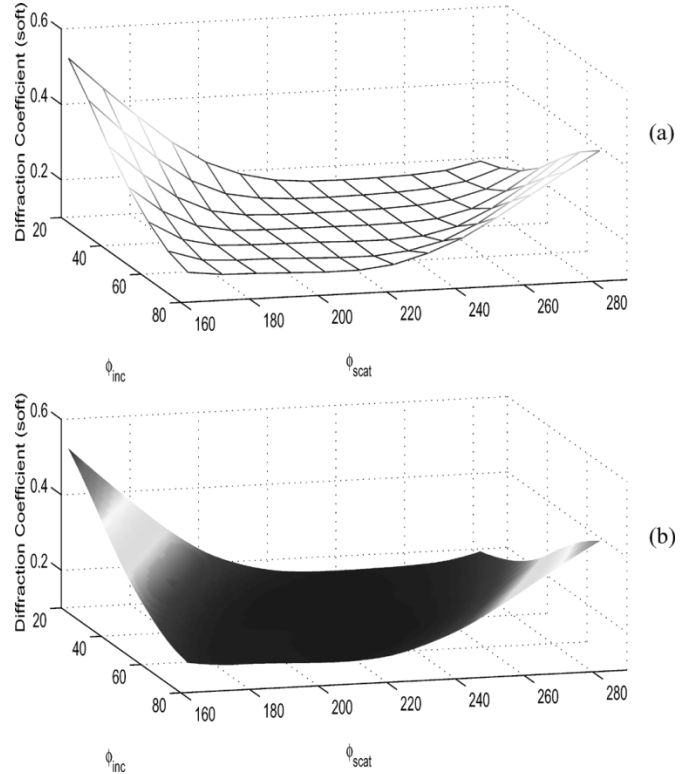


Fig. 7. G-TF/SF FDTD calculated soft diffraction coefficient data set for the 3-D  $\epsilon_r = 6$  dielectric wedge of Fig. 6. (a) Discrete values calculated at  $10^\circ$  increments of  $\phi_{inc}$  and  $\phi_{scat}$  in the range ( $15^\circ \leq \phi_{inc} \leq 75^\circ$ ,  $165^\circ \leq \phi_{scat} \leq 285^\circ$ ) for  $\theta_{inc} = 65^\circ$ . (b) MATLAB interpolation of (a) visualized at  $1^\circ$  increments of  $\phi_{inc}$  and  $\phi_{scat}$ .

## VI. DEVELOPMENT OF A DIFFRACTION COEFFICIENT LIBRARY VIA INTERPOLATION

Finally, we present an efficient means to store G-TF/SF FDTD-calculated diffraction coefficient data for a wide range of incident and diffracted wave angles. We exploit the capability of MATLAB to fit an interpolating hypersurface to multidimensional data, in our case the calculated variation of the diffraction coefficient as a function of the complete set of incident-wave and diffracted-wave propagation angles. As an example, we consider the same 3-D  $\epsilon_r = 6$  dielectric wedge of Fig. 6. Fig. 7(a) is a 3-D surface visualization of a set of soft diffraction coefficient data for this dielectric wedge calculated using G-TF/SF FDTD at  $10^\circ$  increments of  $\phi_{inc}$  and  $\phi_{scat}$  in the range  $15^\circ \leq \phi_{inc} \leq 75^\circ$  and  $165^\circ \leq \phi_{scat} \leq 285^\circ$  for  $\theta_{inc} = 65^\circ$ . Fig. 7(b) shows the corresponding visualization generated by MATLAB using a three-dimensional cubic surface interpolation of the data of Fig. 7(a) at  $1^\circ$  increments of  $\phi_{inc}$  and  $\phi_{scat}$ . Fig. 8(a) and (b) shows the corresponding visualizations for the same dielectric wedge for the hard diffraction coefficients. Finally, Fig. 9 visualizes the soft diffraction coefficient data for incident angles  $25^\circ \leq \theta_{inc} \leq 75^\circ$  and  $15^\circ \leq \phi_{inc} \leq 75^\circ$  for fixed angles  $\theta_{scat} = 30^\circ$  and  $\phi_{scat} = 185^\circ$ .

We see that the problem of generating a library of diffraction coefficients could be greatly simplified. Namely, the G-TF/SF FDTD method would be used to calculate the diffraction coefficients for a particular material wedge over a relatively coarsely sampled set of incident and diffracted wave angles. This small

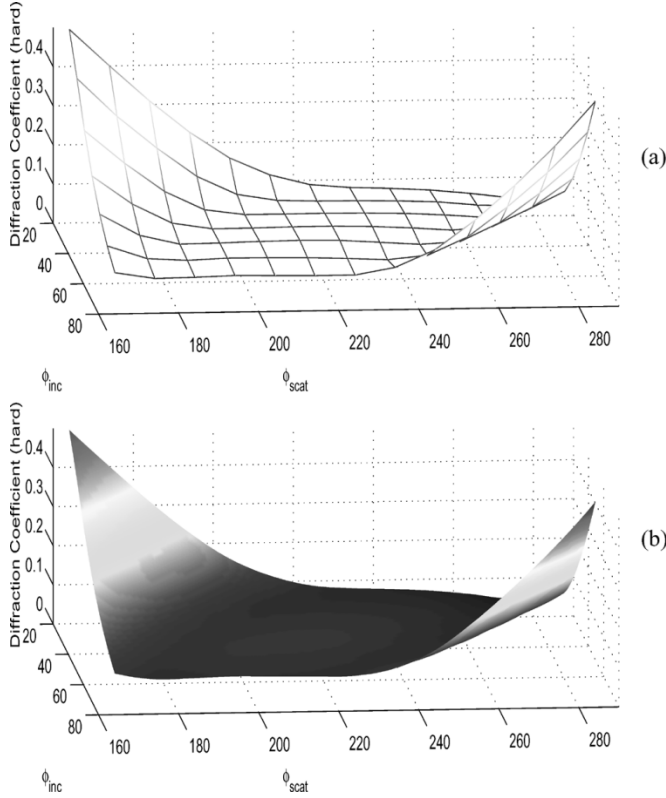


Fig. 8. G-TF/SF FDTD calculated hard diffraction coefficient data set for the 3-D  $\epsilon_r = 6$  dielectric wedge of Fig. 6. (a) Discrete values calculated at  $10^\circ$  increments of  $\phi_{inc}$  and  $\phi_{scat}$  in the range ( $15^\circ \leq \phi_{inc} \leq 75^\circ$ ,  $165^\circ \leq \phi_{scat} \leq 285^\circ$ ) for  $\theta_{inc} = 65^\circ$ . (b) MATLAB interpolation of (a) visualized at  $1^\circ$  increments of  $\phi_{inc}$  and  $\phi_{scat}$ .

set of data would be supplied to a field engineer to be imported to a MATLAB package which would subsequently interpolate the FDTD data to any required resolution. In this manner, the burden of performing the interpolation would fall upon the well-known and widely available commercial software MATLAB.

## VII. CONCLUSION

We have shown that 3-D numerical diffraction coefficients for infinite right-angle material wedges can be efficiently calculated using a generalized total-field/scattered-field FDTD technique. This approach permits modeling an infinite material wedge inside a compact FDTD grid which contains only the volume in the immediate vicinity of the diffracting corner. Our numerical validation results for the PEC wedge show very good correspondence with asymptotic UTD solution. Calculation of diffraction coefficients for the infinite right-angle material wedge having arbitrary permittivity and/or loss is a trivial extension of the PEC wedge case. For the results shown here, the wedge size is reduced by about 4:1 in each dimension relative to the conventional TF/SF method. This yields an approximate 64:1 reduction in computer memory and running time. Finally, MATLAB provides a powerful and straightforward means to compactly store and interpolate the numerical diffraction coefficients over a broad range of propagation angles of the incident and scattered waves. Future work involves extension and validation of the technique for nonright-angle wedges.

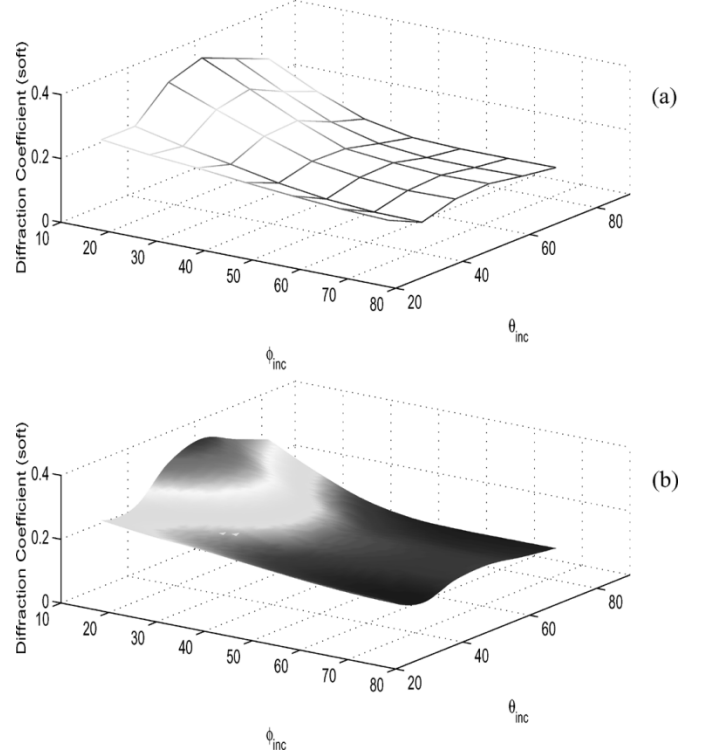


Fig. 9. G-TF/SF FDTD calculated soft diffraction coefficient data set for the 3-D  $\epsilon_r = 6$  dielectric wedge of Fig. 6. (a) Discrete values calculated at  $10^\circ$  increments of  $\phi_{inc}$  and  $\theta_{inc}$  in the range ( $15^\circ \leq \phi_{inc} \leq 75^\circ$ ,  $25^\circ \leq \theta_{inc} \leq 75^\circ$ ) for fixed angles ( $\phi_{scat} = 185^\circ$ ,  $\theta_{scat} = 30^\circ$ ). (b) MATLAB interpolation of (a) visualized at  $1^\circ$  increments of  $\phi_{inc}$  and  $\theta_{inc}$ .

## APPENDIX A

### UNIFORM THEORY OF DIFFRACTION FOR AN INFINITE RIGHT-ANGLE PEC WEDGE

In Fig. 10(a), a plane wave is incident at an oblique angle  $\beta'_o$  to the PEC wedge. This generates a cone of diffracted rays starting from  $P_d$  at an angle  $\beta_o = \beta'_o$  with respect to the edge. All the observation point ( $P_o$ ) lying on this cone obeys the Keller's *law of diffraction* [9],  $\beta_o = \beta'_o$ . By choosing appropriate ray-fixed coordinates, the diffracted-ray field is obtained as [5], [8]

$$\begin{bmatrix} E_{\beta'_o}^d(s) \\ E_{\phi'}^d(s) \end{bmatrix} = - \begin{bmatrix} D_s & 0 \\ 0 & D_h \end{bmatrix} \begin{bmatrix} E_{\beta'_o}^i(P_d) \\ E_{\phi'}^i(P_d) \end{bmatrix} \frac{1}{\sqrt{s}} e^{-j\beta s} \quad (A1)$$

where the incident field components are

$$E_{\beta'_o}^i(P_d) = \hat{\beta}'_o \cdot \vec{E}_i \quad (A2a)$$

$$E_{\phi'}^i(P_d) = \hat{\phi}' \cdot \vec{E}_i. \quad (A2b)$$

The uniform diffraction coefficients  $D_s$  and  $D_h$  are given by (A3a) and (A3b) at the bottom of the next page, where  $\xi^+ = \phi + \phi'$ ,  $\xi^- = \phi - \phi'$ ,  $F(X)$  is Fresnel's transition function, and  $L = s \sin^2 \beta'_o$ .

## APPENDIX B

### 3-D DIFFRACTION COEFFICIENTS DERIVED USING FDTD

Fig.10(b) shows the 3-D geometry of the scatterer used in the FDTD modeling and the relationship between the FDTD coordinate system and the ray-fixed coordinate system. This figure shows the edge-fixed plane of incidence ( $\hat{s}'$ ,  $\hat{e}$ ) with the ray-fixed unit vectors  $\hat{\beta}'_o$  and  $\hat{\phi}'$  parallel and perpendicular to it,

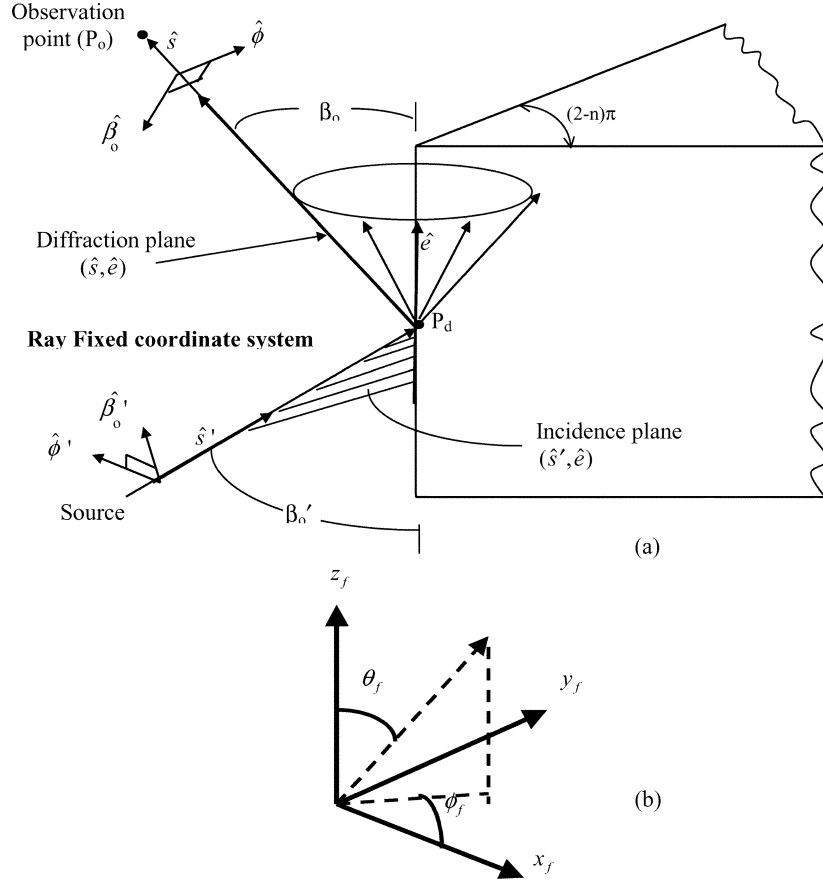


Fig. 10. (a) 3-D geometry of an infinite right-angle wedge illuminated by a plane wave at oblique incidence. The edge-fixed plane of incidence and diffraction, the ray-fixed coordinate system, and (b) the FDTD coordinate system are shown.

respectively. Also shown is the edge-fixed plane of diffraction  $(\hat{s}, \hat{e})$  with the ray-fixed unit vectors  $\hat{\beta}_o$  and  $\hat{\phi}$  parallel and perpendicular to it, respectively. The edge-fixed spherical angles made by the incident ray and the diffracted ray are  $(\beta'_o, \phi'_o)$  and  $(\beta_o, \phi)$ , respectively. The FDTD coordinate system  $(\hat{i}_f, \hat{j}_f, \hat{k}_f)$  is parallel to the three orthogonal edges of the scatterer.

We find the diffracted-field impulse response of the scatterer numerically using FDTD. By illuminating the wedge with a pulsed plane wave having an electric field (E-field) component parallel to the plane of incidence, we obtain the diffracted-field impulse response  $h_{\beta_o, \text{num}}$  polarized parallel to the plane of diffraction. An analogous procedure is performed with the incident E-field component perpendicular to the plane of incidence, yielding  $h_{\phi, \text{num}}$  polarized perpendicular to the plane of diffraction. The Fourier transforms of these diffracted-field impulse responses,  $H_{\beta_o, \text{num}}$  and  $H_{\phi, \text{num}}$ , give the corresponding spectra of the diffracted fields. The diffracted-ray field given by the UTD in terms of the scalars  $D_s$  and  $D_h$  is shown in (A3a)

and (A3b), respectively. This indicates that the FDTD-computed diffraction coefficients,  $D_{s, \text{FDTD}}$  and  $D_{h, \text{FDTD}}$ , can be found using

$$D_{s, \text{FDTD}}(s, \theta, \phi, \omega) = H_{\beta_o, \text{num}}(s, \theta, \phi, \omega) \sqrt{s} e^{jk_o s} \quad (\text{B1a})$$

$$D_{h, \text{FDTD}}(s, \theta, \phi, \omega) = H_{\phi, \text{num}}(s, \theta, \phi, \omega) \sqrt{s} e^{jk_o s} \quad (\text{B1b})$$

where  $s$  is the distance of the observation point from the scattering edge and  $k_o = \omega \sqrt{\mu_0 \epsilon_0}$ . The Fourier transform has been defined using the  $e^{-j\omega t}$  convention. The factor,  $\sqrt{s} e^{jk_o s}$ , in the above equation arises from the nature of the Green's function in two dimensions.  $H_{\beta_o, \text{num}}$  and  $H_{\phi, \text{num}}$  can be obtained using

$$H_{\beta_o, \text{num}}(s, \theta, \phi, \omega) = \frac{\Im \left\{ \vec{E}_{\text{dif}}^{\text{num}}(t, s, \theta_f^d, \phi_f^d) \cdot \hat{\beta}_o \right\}}{\Im \left\{ \vec{E}_{\text{inc}}^{\text{num}}(t, 0, \theta_f^i, \phi_f^i) \cdot \hat{\beta}'_o \right\}} \quad (\text{B2a})$$

$$H_{\phi, \text{num}}(s, \theta, \phi, \omega) = \frac{\Im \left\{ \vec{E}_{\text{dif}}^{\text{num}}(t, s, \theta_f^d, \phi_f^d) \cdot \hat{\phi} \right\}}{\Im \left\{ \vec{E}_{\text{inc}}^{\text{num}}(t, 0, \theta_f^i, \phi_f^i) \cdot \hat{\phi}' \right\}} \quad (\text{B2b})$$

$$D_s(L, \phi, \phi', \omega) = \frac{-e^{-j\frac{\pi}{4}}}{2n\sqrt{2\pi\beta} \sin \beta'_o} \begin{bmatrix} \cot\left(\frac{\pi+\xi^-}{2n}\right) F(\beta L g^+(\xi^-)) + \cot\left(\frac{\pi-\xi^-}{2n}\right) F(\beta L g^-(\xi^-)) \\ -\cot\left(\frac{\pi+\xi^+}{2n}\right) F(\beta L g^+(\xi^+)) - \cot\left(\frac{\pi-\xi^+}{2n}\right) F(\beta L g^-(\xi^+)) \end{bmatrix} \quad (\text{A3a})$$

$$D_h(L, \phi, \phi', \omega) = \frac{-e^{-j\frac{\pi}{4}}}{2n\sqrt{2\pi\beta} \sin \beta'_o} \begin{bmatrix} \cot\left(\frac{\pi+\xi^-}{2n}\right) F(\beta L g^+(\xi^-)) + \cot\left(\frac{\pi-\xi^-}{2n}\right) F(\beta L g^-(\xi^-)) \\ +\cot\left(\frac{\pi+\xi^+}{2n}\right) F(\beta L g^+(\xi^+)) + \cot\left(\frac{\pi-\xi^+}{2n}\right) F(\beta L g^-(\xi^+)) \end{bmatrix} \quad (\text{A3b})$$

where  $\vec{E}_{\text{dif}}^{\text{num}}(t, s, \theta_f^d, \phi_f^d) \cdot \hat{\beta}$  and  $\vec{E}_{\text{dif}}^{\text{num}}(t, s, \theta_f^d, \phi_f^d) \cdot \hat{\phi}$  are, respectively, the components of the diffracted field parallel and perpendicular to the plane of diffraction.  $\vec{E}_{\text{inc}}^{\text{num}}(t, 0, \theta_f^i, \phi_f^i) \cdot \hat{\beta}'_o$  and  $\vec{E}_{\text{inc}}^{\text{num}}(t, 0, \theta_f^i, \phi_f^i) \cdot \hat{\phi}'$  are, respectively, the components of the incident field at the point of diffraction, parallel to and perpendicular to the plane of incidence. Here, the angles  $(\theta_f^i, \phi_f^i)$  represent the direction of the incident plane wave illumination in the FDTD coordinate system. Further, the angles  $(\theta_f^d, \phi_f^d)$  represent the direction of the diffracted ray from the point of diffraction  $P_d$  to the observation point  $P_o$ .

In order to compute the dot products in (B2), we express the ray-fixed unit vectors  $(\hat{\beta}'_o, \hat{\phi}')$  and  $(\hat{\beta}_o, \hat{\phi})$  in terms of the FDTD unit vectors  $(\hat{i}_f, \hat{j}_f, \hat{k}_f)$  as follows:

$$\hat{\beta}'_o = -\cos \theta_f^i \cos \phi_f^i \hat{i}_f - \cos \theta_f^i \sin \phi_f^i \hat{j}_f + \sin \theta_f^i \hat{k}_f \quad (\text{B3a})$$

$$\hat{\phi}' = -\sin \phi_f^i \hat{i}_f + \cos \phi_f^i \hat{j}_f \quad (\text{B3b})$$

$$\hat{\beta}_o = \cos \theta_f^d \cos \phi_f^d \hat{i}_f + \cos \theta_f^d \sin \phi_f^d \hat{j}_f - \sin \theta_f^d \hat{k}_f \quad (\text{B3c})$$

$$\hat{\phi} = \sin \phi_f^d \hat{i}_f - \cos \phi_f^d \hat{j}_f. \quad (\text{B3d})$$

From (B1) and (B2), it is clear that the FDTD computed diffraction coefficients are obtained using [7]

$$D_{s,\text{FDTD}}(s, \theta_f^d, \phi_f^d, \omega) = \frac{\Im \left\{ \vec{E}_{\text{dif}}^{\text{num}}(t, s, \theta_f^d, \phi_f^d) \cdot \hat{\beta}_o \right\}}{\Im \left\{ \vec{E}_{\text{inc}}^{\text{num}}(t, \theta_f^i, \phi_f^i) \cdot \hat{\beta}'_o \right\}} \sqrt{se^{jk_o s}} \quad (\text{B4a})$$

$$D_{h,\text{FDTD}}(s, \theta_f^d, \phi_f^d, \omega) = \frac{\Im \left\{ \vec{E}_{\text{dif}}^{\text{num}}(t, s, \theta_f^d, \phi_f^d) \cdot \hat{\phi} \right\}}{\Im \left\{ \vec{E}_{\text{inc}}^{\text{num}}(t, \theta_f^i, \phi_f^i) \cdot \hat{\phi}' \right\}} \sqrt{se^{jk_o s}}. \quad (\text{B4b})$$

## REFERENCES

- [1] V. Anantha and A. Taflove, "Efficient modeling of infinite scatterers using a generalized total-field/scattered-field FDTD boundary partially embedded within PML," *IEEE Trans. Antennas Propag.*, vol. 50, no. 10, pp. 1337–1349, Oct. 2002.
- [2] A. Taflove and S. Hagness, *Computational Electrodynamics: The Finite-Difference-Time-Domain Method*. Boston, MA: Artech House, 2000.
- [3] T. Martin and L. Pettersson, "Dispersion compensation for Huygens' sources and far-zone transformation in FDTD," *IEEE Trans. Antennas Propag.*, vol. 48, no. 4, pp. 494–501, Apr. 2000.
- [4] C. D. Moss, F. L. Teixeira, and J. A. Kong, "Analysis and compensation of numerical dispersion in the FDTD method for layered, anisotropic media," *IEEE Trans. Antennas Propag.*, vol. 50, no. 9, pp. 1174–1184, Sep. 2002.
- [5] R. G. Kouyoumjian and P. Pathak, "A uniform geometrical theory of diffraction for an edge in perfectly conducting surface," *Proc. IEEE*, vol. 62, no. 11, pp. 1448–1461, November 1974.
- [6] J. P. Berenger, "A perfectly matched layer for the absorption of electromagnetic waves," *J. Computational Phys.*, vol. 114, pp. 185–200, 1994.
- [7] J. Chang, "Diffraction models for accurate RF propagation predictions in urban environments," Ph.D. dissertation, Northwestern Univ., 2004.
- [8] C. A. Balanis, "Geometrical theory of diffraction," in *Advanced Engineering Electromagnetics*. New York: Wiley, 1989, ch. 13.
- [9] J. B. Keller, "Geometrical theory of diffraction," *J. Opt. Soc. Amer.*, vol. 52, no. 2, pp. 116–130, Feb. 1962.



**Juan-Her Chang** received the B.S. degree in physics from National Taiwan Normal University, Taiwan, R.O.C., in 1993, the M.S. degree in physics, and the Ph.D. degree in electrical and computer engineering from Northwestern University, Evanston, IL, in 1998 and 2004, respectively.

Since 1999, she has been a Research Assistant in the Electrical and Computer Engineering Department at Northwestern University.



**Allen Taflove** (F'90) was born in Chicago, IL, on June 14, 1949. He received the B.S., M.S., and Ph.D. degrees in electrical engineering from Northwestern University, Evanston, IL, in 1971, 1972, and 1975, respectively.

After nine years as a Research Engineer at the IIT Research Institute, Chicago, IL, he returned to Northwestern in 1984. Since 1988, he has been a Professor in the Department of Electrical and Computer Engineering, McCormick School of Engineering, Northwestern. Since 1972, he has pioneered basic theoretical approaches and engineering applications of finite-difference time-domain (FDTD) computational electrodynamics. He coined the FDTD acronym in a 1980 IEEE paper, and in 1990 was the first person to be named a Fellow of IEEE in the FDTD area. Currently, FDTD is one of the most powerful and widely used methods for solving Maxwell's equations to model linear and nonlinear electromagnetic wave interactions with electrically large and complex structures. In 1995, he authored a popular textbook on this subject *Computational Electrodynamics: The Finite-Difference Time-Domain Method* (Boston, MA: Artech House, 1995), which is now in its second edition (2000), with a third edition is planned for 2005. In total, he has authored or co-authored four books, 20 book chapters and magazine articles, 92 refereed journal papers, approximately 200 conference papers and abstracts, and 14 U.S. patents. These publications resulted in his being included in *ISI Highly Cited.com*, the Institute of Scientific Information's compilation of the most-cited researchers worldwide. He has been the thesis adviser of 18 Ph.D. recipients who hold professorial or technical staff positions at major institutions including research universities and national labs. Currently, he serves as the faculty Master of Northwestern's 140-student Slivka Residential College of Science and Engineering. He also serves as the Faculty Advisor to Northwestern's Undergraduate Design Competition, the student chapters of the Eta Kappa Nu and Tau Beta Pi engineering honor societies, and McCormick's Honors Program in Undergraduate Research. His efforts on behalf of students at all levels were recognized by Northwestern when he was named a C. D. McCormick Professor of Teaching Excellence in 2000. His research interests span much of the electromagnetic spectrum. He and his students are currently modeling electrodynamic phenomena ranging from geophysically induced extremely low frequency wave propagation about the entire Earth to the lasing behavior of aggregates of micron-scale zinc-oxide particles exhibiting four-level quantum-system characteristics. The principle that "Maxwell's equations work from dc to light" is vividly demonstrated in his laboratory every day.